Chemical Science

Accepted Manuscript

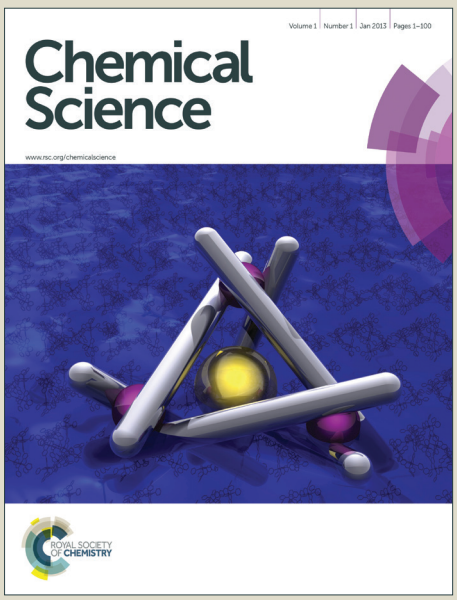

ROYAL SOCIETY OF CHEMISTRY

www.rsc.org/chemicalscience

Asymmetric Supercapacitors with High Energy Density Based on Helical Hierarchical Porous Na_xMnO_2 and MoO_2

Xue-Feng Lu, Zhi-Xiang Huang, Ye-Xiang Tong, and Gao-Ren Li*

MOE Laboratory of Bioinorganic and Synthetic Chemistry, KLGHEI of Environment and Energy Chemistry, School of Chemistry and Chemical Engineering, Sun Yat-sen University, Guangzhou 510275, China

School of Chemistry & Chemical Engineering, South China University of Technology, Guangzhou 510640, China

E-mail: ligaoren@mail.sysu.edu.cn

The helical hierarchical porous Na_xMnO_2/CC and MoO_2/CC, which are assembled from nanosheets and nanoparticles, respectively, are fabricated by a simple electrodeposition method. These unique helical porous structures enable electrodes high capacitance and outstanding cycling performance. Based on the helical Na_xMnO_2/CC as positive electrodes and helical MoO_2/CC as negative electrodes, high performance Na_xMnO_2/CC//MoO_2/CC asymmetric supercapacitors (ASCs) are successfully assembled, and they achieve a maximum volume C_{sp} of 2.04 F cm^{-3} and a maximum energy density of 0.92 mWh cm^{-3} for the whole device and excellent cycling stability with 97.22% C_{sp} retention after 6000 cycles.

Keywords: Helical structure, porous structure, metal oxide, asymmetric supercapacitor, energy storage

1. INTRODUCTION

Increasing demands in portable electronics and future green transportation are pursing the research to electrochemical energy storage (EES) systems with high energy density, high power density and long cycling life.[1] Electrochemical capacitors, also known as supercapacitors, bridge the gap between batteries and conventional capacitors in terms of their high power density and have been regarded as the most promising EES device.[2] However, their energy density is still relatively low, which has restricted their potential applications. Therefore, the improvement of energy density is crucial for supercapacitors to meet the future energy demands.

As we known, the energy density of a supercapacitor device can be calculated according to the equation $E=1/2C_{sp}V^2$, and and it can be enhanced by maximizing the specific capacitance (C_{sp}) and operation voltage (V).[3] The promising approach for the enhancement of C_{sp} is to develop new electrodes with high C_{sp}.[4] An effective approach to increase the operation voltage is to use organic electrolyte, which can provide a wide voltage window up to 3.0 V. However, they suffer from high cost, poor ionic conductivity and high toxicity, which limit their wide application. In addition, a promising alternative for the operation voltage increase is to develope asymmetric supercapacitors (ASCs), which typically consist of cathodes as energy source and anodes as power source.[5] Compared with symmetric supercapacitors, the ASCs take advantage of different voltage windows of two electrodes in the same electrolyte to increase the device operating voltage and thus significantly improve energy density. In recent decades, intensive efforts have been devoted to explore various ASCs, such as H-TiO_2@MnO_2//H-TiO_2@C (1.8 V),[4] ZnO@MnO_2//rGO (1.8 V),[6] Ni/NiO//rGO (1.5 V),[7] $NiCo_2O_4$//active carbon (1.5 V).[8] Most of ASCs use carbon based-materials as negative electrodes because of their large surface area, excellent electrical conductivity and outstanding stability.[9] However, the low C_{sp} of carbon materials severely limits the energy density of SCs according to the equation of $1/C=1/C_{an}+1/C_{cat}$ (C_{an}: capacitance of anode; C_{cat}: capacitance of cathode). In this regard, some new negative electrodes with high C_{sp}, such as MoO_3,[3a,10] Fe_2O_3,[11] and some metal nitride[12] have been developed for ASCs. But due to the narrow

voltage window, unbalanced capacity between cathode and anode electrodes and unsatisfied cycling stability of metal oxide negative electrodes, there is still a huge challenge to achieve the ASCs with high energy and power densites.

Based on the above considerations, in this paper we designed and synthesized helical hierarchical porous Na_xMnO_2 and MoO_2 on carbon cloth (CC) as positive and negative electrodes, respectively, for ASCs. Manganese oxides have been widely thought to be the most promising material because of their low cost, high abundance, large theoretical C_{sp}, and environment friendly.[13] As a polymorph of MnO_2, the sodium-birnessite-type MnO_2 (Na_xMnO_2) is a two-dimensional layer-structure with bicontinuous networks of solid and pore,[14] and it is an attractive candidate for ASCs as positive electrode material. MoO_2 as nagaive electrode was investigated because of its rich chemistry associated with multiple valence states, low electrical resistivity, natural abundance, and affordable cost.[15] The unique helical hierarchical porous structure of Na_xMnO_2 was assembled from nanosheets and that of MoO_2 were assembled from mesoporous nanoparticles. The helix is a fantastic yet ubiquitous geometry in nature, science, art and architecture, and it exhibits distinctive mechanical, chemical, and physical properties.[16] When the helical structure is used as electrodes for supercapacitors, the appropriate spiral distance and diameter are in favor of electrolyte insertion and thus will improve the utilization ratio of active material. The interspace between two pitches can serve as an "ion reservoir" and further improve the cycling stability of electrodes. The hierarchical porous structure will be much less vulnerable to dissolution, Ostwald ripening and aggregation and will provide large surface area and fast electrolyte penetration/diffusion. Besides, the hierarchical porous structure also can well buffer the volume change to avoid structure collapse of electrodes during the charge/discharge process. The electrochemical measurements demonstrate that the helical hierarchical porous Na_xMnO_2 shows a maximal areal capacitance of 329.69 mF cm^{-2} with a potential window of 0~1.0 V and the helical hierarchical porous MoO_2 shows a maximal areal C_{sp} of 174.97 mF cm^{-2} with a potential window of -1.1~0 V. The ASC device was assembled based on the helical hierarchical porous Na_xMnO_2/CC as positive electrode and helical hierarchical porous MoO_2/CC as negative electrode, and it shows a high volume C_{sp} of 2.04 F cm^{-3}

and a high energy density of 0.92 mWh cm^{-3} based on the whole device. Meanwhile, such an ASC device exhibits a high cycling life with 97.22% C_{sp} retention after 5000 cycles. The present encouraging findings will open up a new opportunity for the development of ASCs with high energy and power densities.

2. EXPERIMENTAL SECTION

Preparation of electrode materials: All the chemical reagents used in this study were of analytical grade (AR). The electrodeposition was carried out in a simple two-electrode cell via galvanostatic electrolysis and the graphite electrode was used as a counter electrode (spectral grade). Carbon cloth was used as the working electrode for the electrodeposition and it was washed with ethanol and water successively in ultrasonic bath for 5 min. The helical Na_xMnO_2 was electrodeposited on caron cloth in a 15 mL solution of 0.02 M $Mn(CH_3COO)_2$+0.2 M Na_2SO_4 at a current density of 4.0 mA cm^{-2} on the anode at room temperature for 10 min. The electrodeposition process is expressed as follows:[14,19]

$$Mn^{2+} + 2\ H_2O + x\ Na^+ \rightarrow Na_xMn^{3+}{}_yMn^{4+}{}_{(1-y)}O_2 + 4\ H^+ + (2-x)\ e^- \quad (1)$$

The helical MoO_2 was electrodeposited in a 15 mL solution of 0.01 M $(NH_4)_6Mo_7O_{24}$ at a current density of 4.0 mA cm^{-2} in cathode at room temperature for 30 min followed by a annealed process in NH_3 atmosphere. The electrodeposition process is expressed as follows:

$$6NH_4^+ + Mo_7O_{24}^{6-} + (18-7x)\ H_2O + (42-14x)\ e^- \rightarrow 7MoO_x + 6\ NH_3 + (42-14x)\ OH^- \quad (2)$$

Fabrication of ASCs: The ASC device was assembled using a helical Na_xMnO_2/CC as positive electrode and helical MoO_2/CC as negative electrode with a separator (NKK separator; Nippon Kodoshi Corporation, Kochi, Japan) between the two electrodes. A Na_2SO_4 aqueous solution (1.0 M) was used as the electrolyte. To avoid leakage of the electrolyte, the entire device was sealed by two pieces of PET membranes with a small part of electrode kept outside.

Material Characterizations and Electrochemical Measurements: The morphologies, microstructures and compositions of the products were characterized by field-emission scanning electron microscopy (FE-SEM, JSM-6330F), X-ray diffractometry (XRD, D-MAX 2200 VPC), transmission electron microscopy (TEM, Tecnai™ G2 F30), and X-ray photoelectron spectroscopy (XPS, ESCALab250). Inductively

coupled plasma atomic emission spectroscopy (ICP, SPECTRO) was used to analyze the loading of the active materials. The electrochemical measurements of the electrodes were carried out in a standard three-electrode electrolytic cell in a 1.0 M Na_2SO_4 aqueous solution. A graphite electrode was used as a counter electrode. A saturated calomel electrode (SCE) was used as the reference electrode. The cyclic voltammometry and chronopotentiometric measurements were performed on a CHI 760E electrochemical workstation (CH instruments, Inc.) to determine the electrochemical properties. The EIS was conducted in the frequency range between 0.01 Hz and 100 kHz with amplitude of 5 mV at the open-circuit potential.

3. RESULTS AND DISCUSSION

As shown in Scheme 1, the electrodeposition method was used to fabricate the helical hierarchical porous Na_xMnO_2 and MoO_2, which were directly grown on the carbon cloth without binder (the details were described in Experimental Section). SEM images of Na_xMnO_2 with different magnifications were shown in Figure 1a and Figure S1a, which show the perfect and uniform helical structures grown on carbon fibers. More interestingly, a magnified SEM image in Figure 1b shows that the helical structures consist of nanosheets. The thickness of these nanosheets are 15~20 nm. TEM images of Na_xMnO_2 are shown in Figure 1c and Figure S1b, which clearly show the porous structures. HRTEM image in Figure 1d shows the lattice spacings of 0.697, 0.349 and 0.252 nm, which correspond to (001), (002) and (100) crystal planes of Na_xMnO_2, respectively.[17] SAED pattern in the inset of Figure 1c also shows the polycrystalline structure of Na_xMnO_2. A cross-section SEM image in Figure S2 shows that the thickness of helical microstructures is ~1.0 μm. The surface electronic state and chemical composition of the helical Na_xMnO_2 was examined by XPS spectrum. XPS survey spectrum of helical Na_xMnO_2 is shown in Figure S3, which shows the existences of elements Mn, O, Na and C. The signals of C come from carbon cloth substrate. The atomic ratio of Na/Mn is about 1/10, which is confirmed by the energy dispersive X-ray spectroscopy (EDX) as shown in Figure S4. In the Mn 2p spectra (Figure 1e), two kinds of manganese species containing Mn^{3+} and Mn^{4+} can be observed. The fitting peaks at 641.45 eV

and 653.15eV are indexed to Mn^{3+}, while the fitting peaks at 642.61 eV and 654.31 eV are indexed to Mn^{4+}.[18] Additionally, the Mn 3s peaks are useful for determining the oxidation state of Mn. In Figure 1f, the energy separation between two peaks of Mn 3s is 4.8 eV, which corresponds to an average Mn oxidation state of ~3.8 according to a linear relationship between manganese oxidation state and ΔE value.[18-19] The atomic ratio of Mn^{3+}/Mn^{4+} in sample is about 1/4. The O 1s spectrum shown in Figure 1g is deconvoluted into three components. The bands at 529.9, 531.3 and 533.1 eV can be assigned to the oxygen bonds of Mn-O-Mn, Mn-O-H and H-O-H, respectively.[19] The bond of Mn-O-Mn comes from Na_xMnO_2 and those of Mn-O-H and H-O-H can be attributed to the adsorbed H_2O or crystal H_2O. Based on the above results, the composition of the sodium-birnessite-type manganese oxide can be identified as $Na_{0.1}MnO_2$ ($Na_{0.1}Mn^{3+}_{0.2}Mn^{4+}_{0.8}O_2$).

Cyclic voltammetry (CV) and galvanostatic charge-discharge (GCD) are generally used to characterize the capacitance behavior of an electrode material. Figure 2a-b shows the typical CV and GCD curves of the helical Na_xMnO_2/CC at different scan rates and current densities, respectively, in 1.0 M Na_2SO_4 solution. In the potential of 0~1.0 V, the behavior of helical Na_xMnO_2/CC slightly deviates from the ideal rectangular shape with a small and broad redox couple, indicating the pseudocapacitance properties of Na_xMnO_2/CC. These redox peaks can be definitely ascribed to the intercalation-deintercalation of Na^+ into and from the solid MnO_2 lattice.[14, 19-20] GCD curves of helical Na_xMnO_2/CC are almost linear and symmetrical without an obvious IR drop as shown in Figure 2b, indicating a rapid *I-V* response and good capacitance performance. The areal C_{sp} of the helical Na_xMnO_2/CC obtained from GCD curves is shown in Figure 2c, which shows that the highest C_{sp} is 329.69 mF cm^{-2} at a current density of 0.29 mA cm^{-2}. The C_{sp} value of 329.69 mF cm^{-2} is much higher than those of other MnO_2 electrodes reported in the literatures (10~100 mF cm^{-2}).[4,21] In addition, the helical Na_xMnO_2/CC electrode has a small charge-transfer resistance (R_{ct}) of ~1.5 Ω as shown in Figure 2d, suggesting the fast charge transfer and transport process.[22] Figure S7 shows excellent cycling stability of the helical Na_xMnO_2/CC and a high C_{sp} retention of 99.97% after 5000 cycles is achieved. In addition, Figure S8 shows EIS spectra of the helical Na_xMnO_2/CC before and after 5000 cycles, from which we can see that

the charge-transfer resistance is almost unchanged after 5000 cycles.

The helical MoO_2/CC as negative electrode is fabricated as shown in Figure 3a. The helical structure is constructed by nanoparticles with diameters of 100~200 nm as shown in Fiugre 3b and Figure S9a. TEM image of MoO_2 is shown in Figure S9b, which clearly shows the porous structures. The thickness of the helical structure is ~3.5μm as shown in Figure S9a. More importantly, the magnified TEM shows these nanoparticles are mesoporous as shown in Figure 3c, which will be beneficial to enhance the specific surface area and thus will provide more active reaction sites. Figure 3d shows HRTEM image of helical MoO_2, in which the lattice spacings of 0.243, 0.240, 0.171 and 0.170 nm correspond to (-211), (-202), (-312) and (-222) crystal planes of MoO_2 (JCPDS#32-0671), respectively.[23] The SAED pattern in the inset of Figure 3c reveals the diffraction rings of typical monoclinic structure of MoO_2, which is in accord with the results of XRD pattern shown in Figure 3e. All diffraction peaks can be assigned to the monoclinic MoO_2 phase and no diffraction peak comes from other molybdenum oxides such as MoO_3. The survey XPS spectra of MoO_2 electrode is shown in Figure S10, which indicates the presence of Mo, O and C elements in the sample. The atomic ratio Mo/O is about 2, which is consistent with stoichiometric MoO_2 composition. The element C comes from the carbon cloth that is used as substrate. High-resolution XPS spectrum of Mo 3d can be deconvoluted into two doublets as shown in Figure 3f. The binding energies of Mo $3d_{5/2}$ and $3d_{3/2}$ peaks at 229.6 and 232.9 eV indicate the oxidation state of Mo(IV).[24] In addition, the small peaks at 232.5 and 235.6 eV are seen, and they correspond to Mo(VI) $3d_{5/2}$ and $3d_{3/2}$, respectively, indicating the existence of Mo(VI). This can be attributed to the surface partial oxidation of MoO_2 in air.[24-25] XPS spectrum of O 1s is shown in Figure 3g, which shows the main peak at 530.53 eV can be assigned to Mo-O bond. The bands of 531.4 and 533.1 eV correspond to C-O and O-H bonds, respectively, [24-25] and they can be attributed to the adsorbed H_2O on carbon cloth.

The fabricated helical MoO_2/CC electrode owns a perfect capacitance behavior with a wide potential window of -1.1~0 V (*vs* SCE) in solution of 1.0 M Na_2SO_4. The wide potential window may be the result of high overpotential of H_2 and O_2 evolution which is related to the structure and property of electrode material.[26] Figure 4a-b shows CV and GCD curves of helical MoO_2/CC, respectively, which

are symmetric and linear, respectively, without an obvious IR drop, indicating good capacitance performance. As shown in Figure 4c, the highest areal C_{sp} obtained from GCD curves is 174.97 mF cm^{-2} at a current density of 1.43 mA cm^{-2}, which is much larger than those of other metal oxide/nitride negative electrodes, such as α-Fe_2O_3,[27] MoO_3,[28a] and VN.[12a,28b] The kinetic features of helical MoO_2/CC electrode was further investigated by measuring the EIS spectrum as shown in Figure 4d, which shows a small bulk solution resistance (R_s) of 7.5 Ω,[29] small charge-transfer resistance (R_{ct}) of 0.5 Ω, and fast ion diffusion into the inner of MoO_2/CC electrode.[30] Morever, the helical MoO_2/CC shows a high cycling stability with a C_{sp} retention of 91.62% after 5000 cycles as shown in Figure S12. To evalute the change of charge-trnsfer resistance, we compared the EIS spectra of helical MoO_2/CC before and after cycling test as shown in Figure S13, from which we can see that the charge-transfer resistance of electrode becomes a little bigger after 5000 cycles.

The flexible asymmetric supercapacitor (ASC) device was assembled using helical Na_xMnO_2/CC as positive electrode and helical MoO_2/CC as negative electrode (Na_xMnO_2/CC//MoO_2/CC ASC). Figure 5a shows the schematic structure of Na_xMnO_2/CC//MoO_2/CC ASC, which is sealed by two thin pieces of PET membrane. Taking advantage of different potential windows of Na_xMnO_2/CC and MoO_2/CC electrodes (Figure S14a), the operating cell potential of the assembled ASCs is expected to be 2.1 V. However, a faradic reaction is observed in the CV and GCD curves beyond the potential of 1.8 V. As shown in Figure S14b, an oxidation peak is observed beyond 1.8 V, highlighted by dashed box, which is also observed in the GCD curves (Figure S14c). When the ASC devices were tested in the potential windows of 2.0 and 2.1 V for 6000 cycles, their capacitance retention is only 63.01% and 40.25%, respectively, as shown in Figure S14d. However, when tested in a potential window of 1.8 V, the ASC has a good cycling stability with a much higher capacitance retention of 97.22%, which is significantly better than those reported in previous work (typically 70-85% retention over 1000 cycles).[26a,32]

Figure 5b shows CVs of an optimized Na_xMnO_2/CC//MoO_2/CC ASC at different scan rates with a potential window of 0~1.8 V in 1.0 M Na_2SO_4 electrolyte. These CVs exhibit rectangular-like shapes, revealing an ideal capacitive behavior and a fast charge/discharge property. As shown in Figure 5c, GCD

curves at different current densities all are reasonably symmetric and show a good linear relation of charge/discharge voltage versus time particularly at a low current density. This result also indicates the ideal capacitive characteristic and rapid charge/discharge property of the assembled ASC device. The volumetric C_{sp} calculated by the discharging curves is shown in Figure S15, which shows a highest C_{sp} of 2.04 F cm^{-3} at 0.57 mA cm^{-2}. The C_{sp} of 2.04 F cm^{-3} is much larger than those of ASCs reported recently.[4,11a,12a,31] In order to demonstrate the flexibility, we measured CVs of the assembled ASCs with different bending angles from 0° to 180° at a scan rate of 100 mV s^{-1}. As shown in Figure 5d and Figure S16, there is no significant C_{sp} loss under the different bending angles, suggesting the excellent flexibility property.

The flexible Na_xMnO_2/CC//MoO_2/CC ASC exhibits a highest energy density of 0.92 mWh cm^{-3} at a power density of 236.15 mW cm^{-3} as shown in Figure 5e. It preserves 36.96% of the highest energy density when the power density increases to the maximal value (483.19 mW cm^{-3}). Here the energy densities are superior to those of previously reported similar ASC systems, including MnO_2//Fe_2O_3 (1.6 V, 0.40 mWh cm^{-3}),[11a] H-TiO_2@MnO_2//H-TiO_2@C (1.8 V, 0.30 mWh cm^{-3}),[4] ZnO@MnO_2//rGO (1.8 V, 0.234 mWh cm^{-3}),[6] and even VO_x//VN (1.8 V, 0.61 mWh cm^{-3}).[12a] To show the practical application, three ASC devices were assembled in series. As shown in Figure 5f, the ASCs can light a SYSU logo consisting of 32 green LEDs, a 50 cm long commercial red (2.0 V) and green (2.5 V) LED soft rope light, indicating high power and energy densities of Na_xMnO_2/CC//MoO_2/CC ASCs.

4. CONCLUSIONS

In summary, we pioneered an electrochemical method for the synthesis of helical Na_xMnO_2/CC and MoO_2/CC with hierarchical porous structures, which are assembled from nanosheets and mesoporous nanoparticles, respectively. These unique electrode structures enable a high working voltage in aqueous, high areal capacitance and outstanding cycling performance. High-performance Na_xMnO_2/CC//MoO_2/CC ASCs based on the helical Na_xMnO_2/CC as positive electrodes and helical MoO_2/CC as negative electrodes are assembled, and they achieve a maximum volume C_{sp} of 2.04 F cm^{-3} and a maximum energy

density of 0.92 mWh cm^{-3} based on the whole device. Furthermore, the Na_xMnO_2/CC//MoO_2/CC ASCs exihibit excellent cycling stability with 97.22% capacitance retention after 6000 cycles. These findings will open a new opportunities for the development of helical hierarchical porous metal oxide electrodes for ASC devices with high energy and power densities.

ACKNOWLEDGMENTS

This work was supported by National Natural Science Foundation of China (51173212 and J1103305), National Basic Research Program of China (2015CB932304), Natural Science Foundation of Guangdong Province (S2013020012833), Fundamental Research Fund for the Central Universities (13lgpy51), SRF for ROCS, SEM ([2012]1707), Project of High Level Talents in Higher School of Guangdong Province, Science and Technology Planning Project of Guangdong Province (2013B010403011) and Open-End Fund of Key Laboratory of Functional Inorganic Material Chemistry (Heilongjiang University), Ministry of Education.

REFERENCES

1 (a) C. Liu, F. Li, L. P. Ma and H. M. Cheng, *Adv. Mater.,* 2010, **22**, 28; (b) G. Yu, L. Hu, M. Vosgueritchian, H. Wang, X. Xie, J. R. McDonough, X. Cui, Y. Cui and Z. Bao, *Nano Lett.,* 2011, **11**, 2905; (c) H. Xia, C. Hong, B. Li, B. Zhao, Z. Lin, M. Zheng, S. V. Savilov and S. M. Aldoshin, *Adv. Funct. Mater.,* 2015, **25**, 627.

2 (a) P. Simon and Y. Gogotsi, *Nat. Mater.* 2008, **7**, 845; (b) J. R. Miller and P. Simon, *Science,* 2008, **321**, 651; (c) R. Liu, F. Wong, W. Duan and A. Sen, *Adv. Mater.,* 2013, **25**, 6997; (c) C. Zhu, P. Yang, D. Chao, X. Wang, X. Zhang, S. Chen, B. K. Tay, H. Huang, H. Zhang, W. Mai and H. J. Fan, *Adv. Mater.*, 2015, **27**, 4566; (d) G. D. Moon, J. B. Joo, M. Dahl, H. Jung and Y. Yin, *Adv. Funct. Mater.,* 2014, **24**, 848.

3 (a) J. Chang, M. Jin, F. Yao, T. H. Kim, V. T. Le, H. Yue, F. Gunes, B. Li, A. Ghosh, S. Xie and Y. H. Lee, *Adv. Funct. Mater.,* 2013, **23**, 5074; (b) P. J. Hall, M. Mirzaeian, S. I. Fletcher, F. B. Sillars, A. J. R. Rennie, G. O. Shitta-Bey, G. Wilson, A. Cruden and R. Carter, *Energy Environ. Sci.,* 2010, **3**, 1238; (c) J. Feng, X. Sun, C. Wu, L. Peng, C. Lin, S. Hu, J. Yang and Y. Xie, *J. Am. Chem. Soc.,* 2011, **133**, 17832.

4 (a) X. Lu, M. Yu, G. Wang, T. Zhai, S. Xie, Y. Ling, Y. Tong and Y. Li, *Adv. Mater.,* 2013, 25, 267; (b) C. Wu, X. Lu, L. Peng, K. Xu, X. Peng, J. Huang, G. Yu and Y. Xie, *Nature Commun.,* 2013, 4, 2431; (c) **H. Xia**, C. Hong, X.

Shi, B. Li, G. Yuan, Q. Yao and J. Xie, *J. Mater. Chem. A,* 2015, 3, 1216; (d) D. Chao, X. Xia, C. Zhu, J. Wang, J. Liu, J. Lin, Z. Shen and H. J. Fan, *Nanocale,* 2014, 6, 5691-5697.

5 (a) X. Lu, M. Yu, G. Wang, Y. Tong and Y. Li, *Energy Environ. Sci.,* 2014, **7**, 2160; (b) J.-X. Feng, S.-H. Ye, A.-L. Wang, X.-F. Lu, Y.-X. Tong and G.-R. Li, *Adv. Funct. Mater.,* 2014, **24**, 7093; (c) C. Zhou, Y. Zhang, Y. Li, and J. Liu, *Nano Lett.*, 2013, **13**, 2078.

6 W. Zilong, Z. Zhu, J. Qiu and S. Yang, *J. Mater. Chem. C,* 2014, **2**, 1331.

7 M. Yu, W. Wang, C. Li, T. Zhai, X. Lu and Y. Tong, *NPG Asia Mater.,* 2014, **6**, 129.

8 X. F. Lu, D. J. Wu, R. Z. Li, Q. Li, S. H. Ye, Y. X. Tong and G. R. Li, *J. Mater. Chem. A,* 2014, 2, 4706.

9 (a) L. Liu, Z. Niu, L. Zhang, W. Zhou, X. Chen and S. Xie, *Adv. Mater.,* 2014, **26**, 4855-4862; (b) L. Dai, D. W. Chang, J. B. Baek and W. Lu, *Small,* 2012, **8**, 1130.

10 G. R. Li, Z. L. Wang, F. L. Zheng, Y. N. Ou and Y. X. Tong, *J. Mater. Chem.,* 2011, **21**, 4217.

11 (a) X. Lu, Y. Zeng, M. Yu, T. Zhai, C. Liang, S. Xie, M. S. Balogun and Y. Tong, *Adv. Mater.,* 2014, **26**, 3148; (b) P. Yang, Y. Ding, Z. Lin, Z. Chen, Y. Li, P. Qiang, M. Ebrahimi, W. Mai, C. P. Wong, Z. L. Wang, *Nano Lett* 2014, **14**, 731.

12 (a) X. Lu, M. Yu, T. Zhai, G. Wang, S. Xie, T. Liu, C. Liang, Y. Tong and Y. Li, *Nano Lett.,* 2013, **13**, 2628; (b) K.-H. Lee, Y.-W. Lee, A. R. Ko, G. Cao, K.-W. Park and B. Vyas, *J. Am. Ceram. Soc.,* 2013, **96**, 37.

13 (a) Q. Li, Z.-L. Wang, G.-R. Li, L.-X. Ding and Y.-X. Tong, *Nano Lett.,* 2012, **12**, 3803; (b) Z.-P. Feng, G.-R. Li, J.-H. Zhong, Z.-L. Wang, Y.-N. Ou and Y.-X. Tong, *Electrochem. Commun.,* 2009, **11**, 706.

14 L. Athouel, F. Moser, R. Dugas, O. Crosnier, D. Belanger and T. Brousse, *J. Phys. Chem. C,* 2008, **112**, 7270.

15 (a) K. M. Hercule, Q. Wei, A. M. Khan, Y. Zhao, X. Tian and L. Mai, *Nano Lett.,* 2013, **13**, 5685; (b) H.-J. Zhang, T.-H. Wu, K.-X. Wang, X.-Y. Wu, X.-T. Chen, Y.-M. Jiang, X. Wei and J.-S. Chen, *J. Mater. Chem. A,* 2013, **1**, 12038.

16 Z. Ren and P. X. Gao, *Nanoscale,* 2014, **6**, 9366.

17 H. Kanoh, W. Tang, Y. Makita and K. Ooi, *Langmuir,* 1997, **13**, 6845-6849.

18 S. R. Das, I. R. Fachini, S. B. Majumder and R. S. Katiyar, *J. Power Sources,* 2006, **158**, 518.

19 M. Nakayama, S. Konishi, H. Tagashira and K. Ogura, *Langmuir,* 2005, **21**, 354.

20 (a) Q. T. Qu, Y. Shi, S. Tian, Y. H. Chen, Y. P. Wu and R. Holze, *J. Power Sources,* 2009, **194**, 1222; (b) Y. K. Zhou, M. Toupin, D. Bélanger, T. Brousse and F. Favier, *J. Phys. Chem. Solids,* 2006, **67**, 1351; (c) M. Nakayama and H. Tagashira, *Langmuir,* 2006, **22**, 3864.

21 (a) Y. Huang, Y. Li, Z. Hu, G. Wei, J. Guo and J. Liu, *J. Mater. Chem. A,* 2013, **1**, 9809; (b) S. W. Lee, J. Kim, S. Chen, P. T. Hammond and Y. Shao-Horn, *ACS Nano,* 2010, **4**, 3889.

22 P. Justin, S. K. Meher and G. R. Rao, *J. Phys. Chem. C,* 2010, **114**, 5203.

23 (a) L. C. Yang, Q. S. Gao, Y. Tang, Y. P. Wu and R. Holze, *J. Power Sources,* 2008, **179**, 357; (b) X. Zhao, M. Cao, B. Liu, Y. Tian and C. Hu, *J. Mater. Chem.,* 2012, **22**, 13334.

24 (a) Q. Qu, T. Gao, H. Zheng, Y. Wang, X. Li, X. Li, J. Chen, Y. Han, J. Shao and H. Zheng, *Adv. Mater. Interfaces,*

2015, **2**, DOI: 10.1002/admi.201500048; (b) Y. Sun, X. Hu, W. Luo and Y. Huang, *ACS Nano,* 2011, **5**, 7100.

25 K. Zhou, W. Zhou, X. Liu, Y. Sang, S. Ji, W. Li, J. Lu, L. Li, W. Niu, H. Liu and S. Chen, *Nano Energy,* 2015, **12**, 510.

26 (a) Z. S. Wu, W. Ren, D. W. Wang, F. Li, B. Liu and H. M. Cheng, *ACS Nano,* 2010, **4**, 5835; (b) C. Xu, H. Du, B. Li, F. Kang and Y. Zeng, *J. Electrochem. Soc.,* 2009, **156**, 435.

27 (a) S. Shivakumara, T. R. Penki and N. Munichandraiah, *ECS Electrochem. Lett.,* 2013, **2**, 60; (b) K. K. Lee, S. Deng, H. M. Fan, S. Mhaisalkar, H. R. Tan, E. S. Tok, K. P. Loh, W. S. Chin and C. H. Sow, *Nanoscale,* 2012, **4**, 2958.

28 (a) Y. Liu, B. Zhang, Y. Yang, Z. Chang, Z. Wen and Y. Wu, *J. Mater. Chem. A,* 2013, **1**, 13582; (b) P. Jampani, A. Manivannan and P. N. Kumta, *Electrochem. Soc. Interface,* 2010, **19**, 57.

29 (a) R. Rakhi, W. Chen, D. Cha and H. Alshareef, *Nano Lett.,* 2012, **12**, 2559; (b) G. Zhang, W. Li, K. Xie, F. Yu and H. Huang, *Adv. Funct. Mater.,* 2013, **23**, 3675.

30 L. Li, Y. Cheah, Y. Ko, P. Teh, G. Wee, C. Wong, S. Peng and M. Srinivasan, *J. Mater. Chem. A,* 2013, **1**, 10935.

31 X. Lu, G. Wang, T. Zhai, M. Yu, S. Xie, Y. Ling, C. Liang, Y. Tong and Y. Li, *Nano Lett.,* 2012, **12**, 5376.

32 S. Chen, J. Zhu, X. Wu, Q. Han and X. Wang, *ACS Nano,* 2010, **4**, 2822.

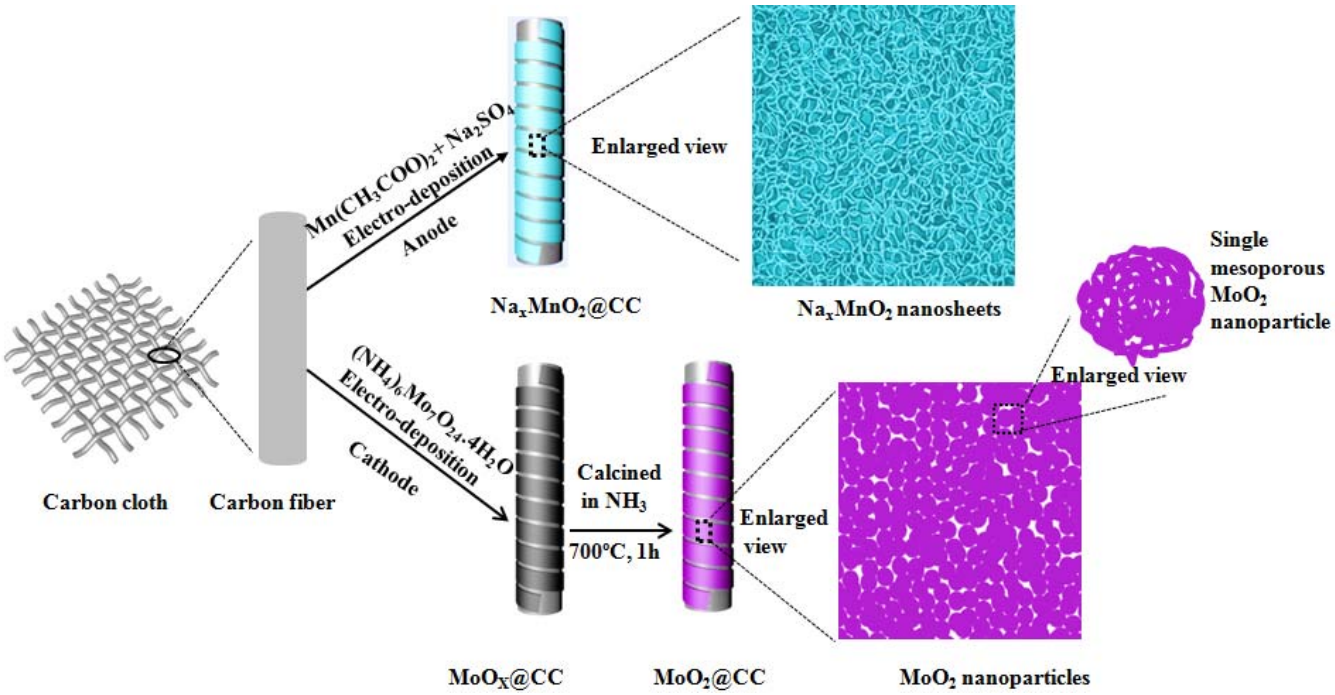

Scheme 1. Representation of the fabrication of helical hierarchical porous Na_xMnO_2/CC and MoO_2/CC.

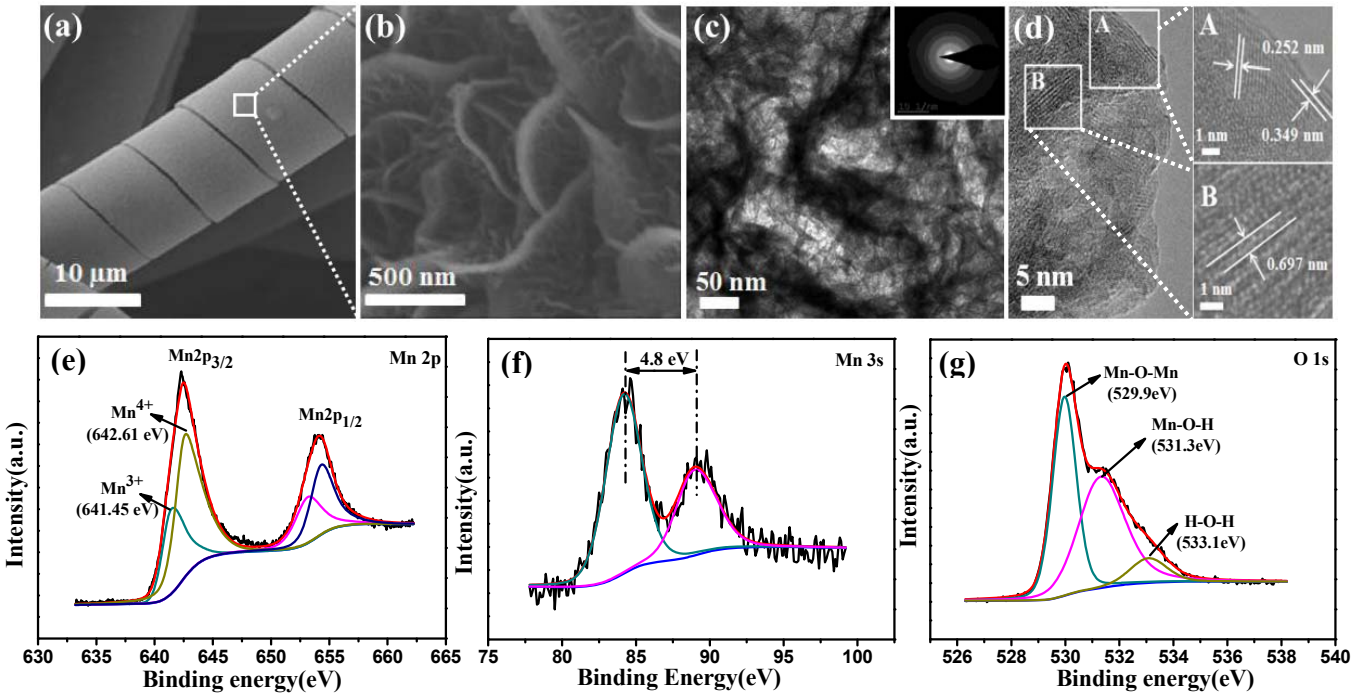

Figure 1. (a-b) SEM images of helical Na_xMnO_2 with hierarchical porous structures; (c) TEM and (d) HRTEM images of the typical Na_xMnO_2 nanosheets (Inset in Figure 1c is SAED pattern); XPS spectra of helical Na_xMnO_2 of (e) Mn 2p, (f) Mn 3s, and (g) O 1s.

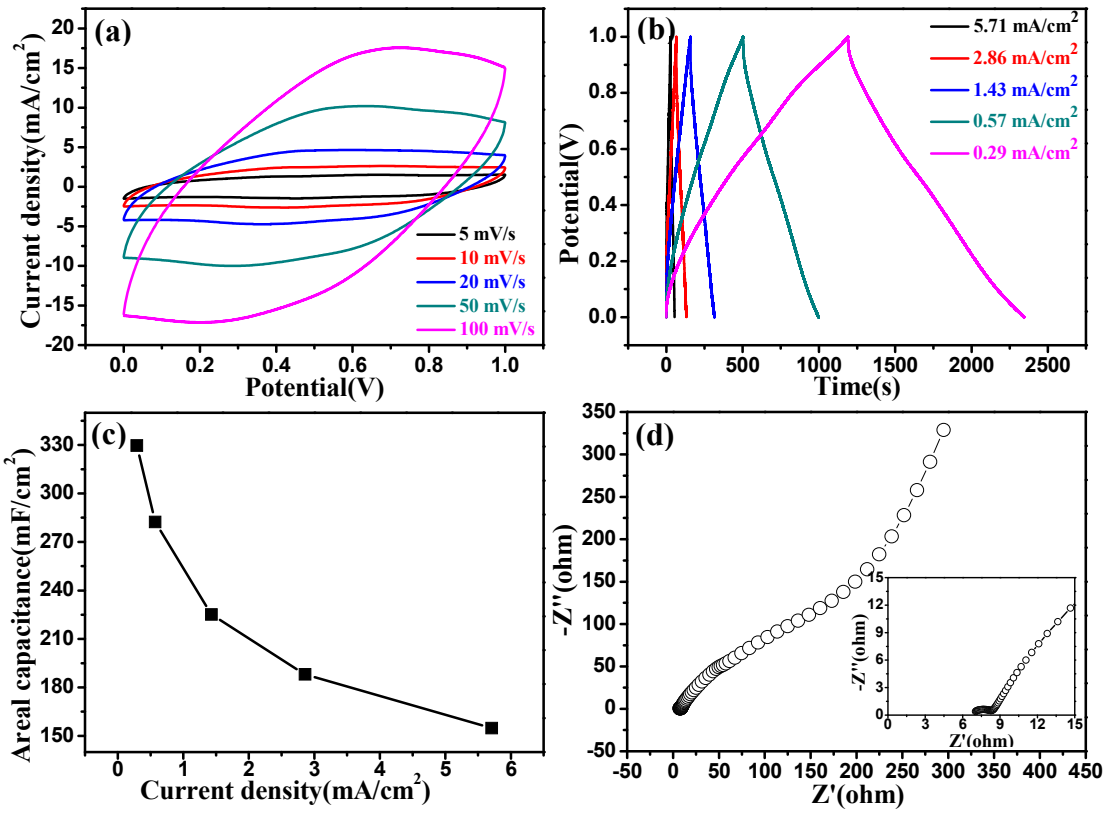

Figure 2. (a) CVs of helical Na_xMnO_2 at different scan rates; (b) GCD curves of helical Na_xMnO_2 at different current densities in 1.0 M Na_2SO_4 electrolyte; (c) Areal capacitance calculated from GCD curves as a function of current densities; (d) EIS spectra of the Na_xMnO_2 (inset is the enlarged view of high frequency region).

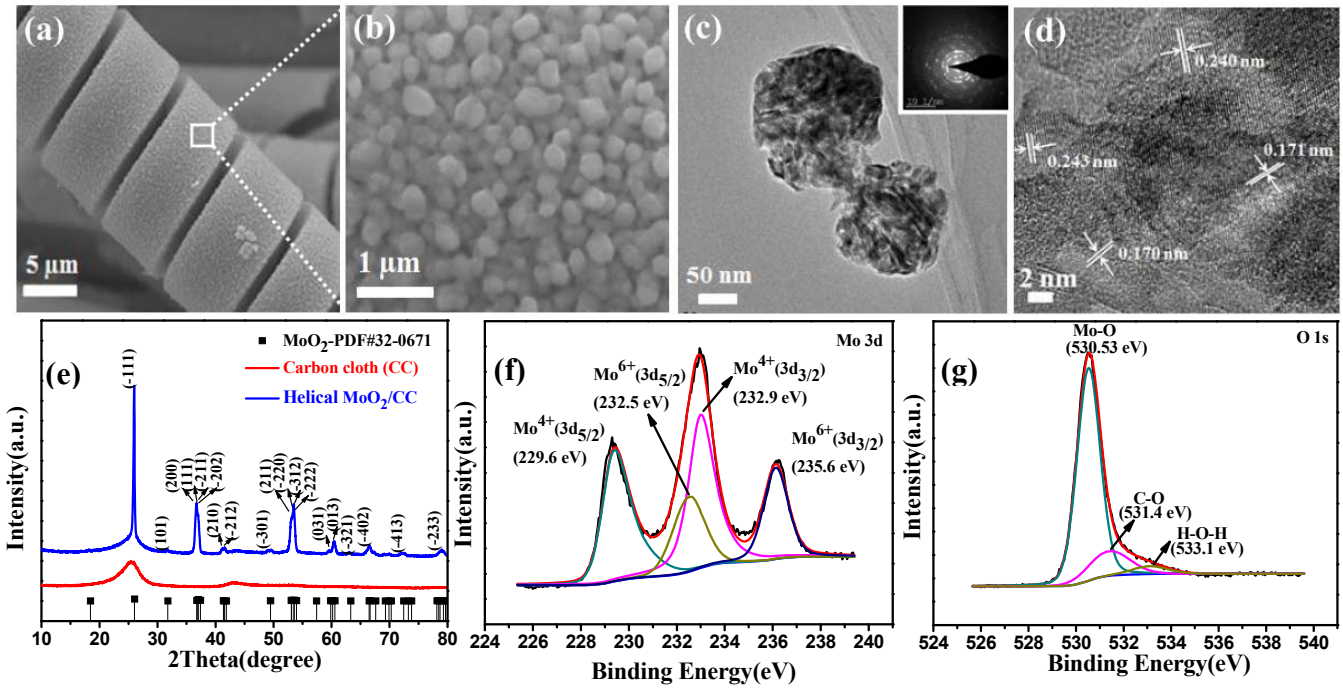

Figure 3. (a-b) SEM images of helical MoO_2 with different magnifications; (c) TEM image of MoO_2 nanoparticles (inset is SAED pattern); (d) HRTEM image of helical MoO_2; (e) XRD patterns of helical MoO_2/CC and CC; XPS spectra of helical MoO_2/CC: (f) Mo 3d and (g) O 1s.

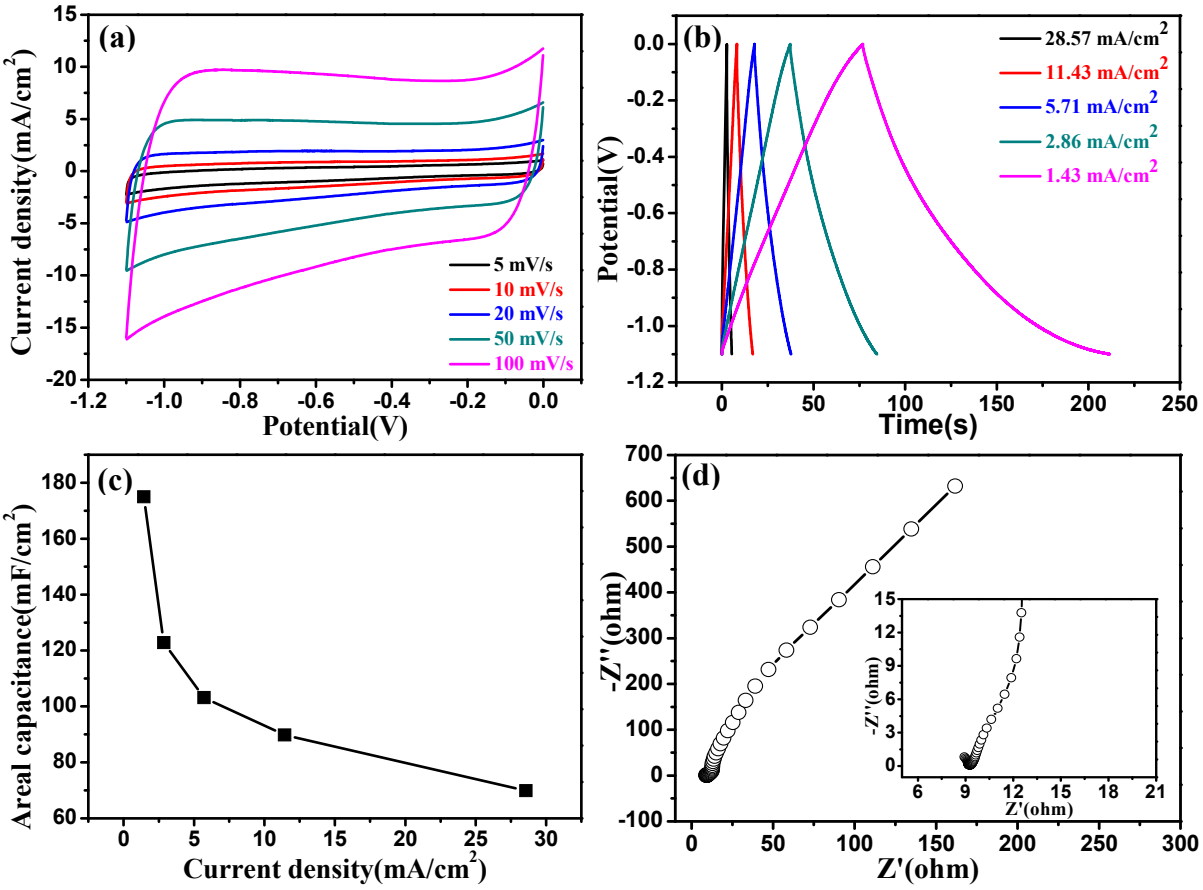

Figure 4. (a) CVs at different scan rates; (b) GCD curves at different current densities of helical MoO_2 in 1.0 M Na_2SO_4 electrolyte; (c) Areal capacitance calculated from GCD curves as a function of current densities; (d) EIS spectra of the MoO_2 (inset is the enlarged view of high frequency region).

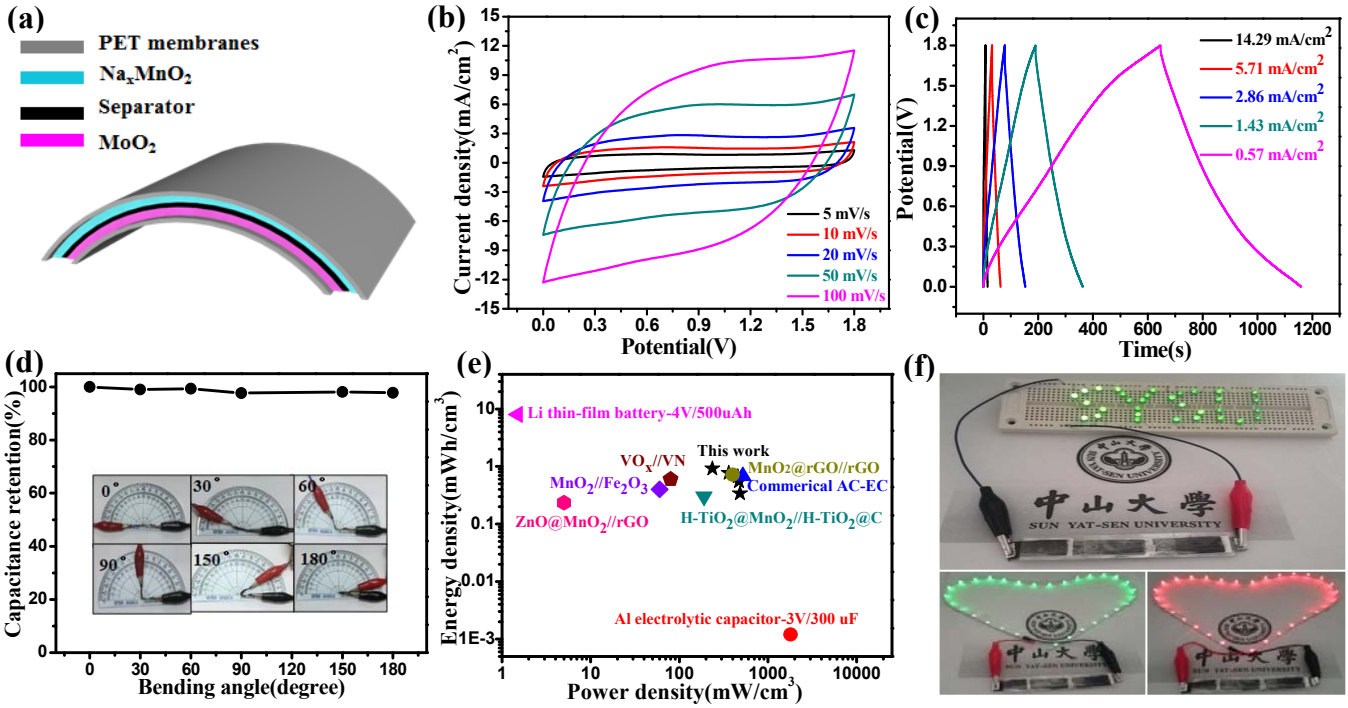

Figure 5. (a) Schematic illustration of the structure of a flexible Na_xMnO_2/CC//MoO_2/CC ASC with two electrodes separated by the TF45 (NKK) membrane (separator); (b) CVs of ASC at different scan rates; (c) GCD curves of ASC at different current densities; (d) stability performance of the ASC collected at different bending angles (the inset shows the flexibility under the different bending angles); (e) Ragone plots of Na_xMnO_2/CC//MoO_2/CC ASC device. The values reported in literatures for other ASC devices are added for comparison; (f) A SYSU logo consisting of 32 green LEDs and a piece of commercial red or green LED soft rope light powered by the assembled ASCs with three in series.

Graphical Abstract Picture